Microporous and Mesoporous Materials 333 (2022) 111705

Contents lists available at ScienceDirect

Microporous and Mesoporous Materials

journal homepage: www.elsevier.com/locate/micromeso

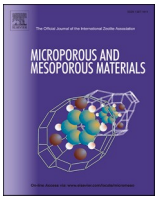

Predicting diffusion barriers and diffusivities of C_6–C_{12} methylbenzenes in MFI zeolites

Mykela DeLuca, David Hibbitts *

Department of Chemical Engineering, University of Florida, Gainesville, FL, 32608, USA

ARTICLE INFO

Keywords:
Diffusion
Aromatics
MFI

ABSTRACT

Mass transport plays an important role in zeolite catalyzed reactions and catalyst deactivation, yet experimental measurement of mass transport, particularly ultra-slow diffusion processes (e.g., of bulky aromatics), is limited because of time scale restraints. Here, we use density functional theory to overcome these limitations and calculate diffusion barriers of benzene and all twelve C_7–C_{12} methylbenzenes through the straight and sinusoidal channels of silicalite-1 (MFI framework). Straight and sinusoidal diffusion barriers are well-predicted by a critical diameter describing the minimum width of the molecule, where benzene, toluene, and *para*-xylene (all 6.6 Å) diffuse through both channels with barriers 200 kJ mol^{-1} lower than those of pentamethylbenzene (8.2 Å). The MFI framework distorts to accommodate species with larger critical diameters and this distortion correlates to activation barriers where smaller molecules, such as benzene, distort the framework to smaller extents compared to larger species, such as pentamethylbenzene. Diffusing through the straight channel of MFI is always more facile than via the sinusoidal channel, by an average of 39 kJ mol^{-1} because the tortuosity of the sinusoidal channels forces larger framework distortions than straight channel diffusion. We show that DFT-calculated straight channel diffusion activation barriers agree well with those reported by frequency response experiments and can be used to calculate self-diffusivities of molecules, with appropriate entropy corrections. Examining all aromatics provides insights to the role of molecule size, channel tortuosity, and entropy during intracrystalline diffusion to provide a reference point for the species that can reasonably diffuse through both channels (e.g., benzene, toluene, xylenes, durene), through straight channels only (e.g., 1,2,3-trimethylbenzene), or simply are 'stuck' within intersections (e.g., pentamethylbenzene) in MFI.

1. Introduction

Proton-form zeolites with medium pores, such as MFI, commonly catalyze reactions involving aromatics—which can be co-fed or formed during reaction—including toluene disproportionation [1–5], Friedel-Crafts acylation [6], xylene isomerization [1,7–11], and methanol-to-hydrocarbons (MTH), olefins (MTO), and gasoline (MTG) [12–16]. Within the MFI framework, straight (5.2 × 5.7 Å, dimensions from IZA) [17] and sinusoidal channels (5.3 × 5.6 Å) intersect to form larger channel intersections (9 Å), where chemistry involving aromatics generally occurs. For example, during MTO aromatics can grow through repeated methylation [18–21], isomerize, and crack to form olefins in the aromatics-based cycle [13,14,16,22–24]. Many of these aromatics are too large to diffuse out of the zeolite crystal and instead react with dienes to grow and form polyaromatics which deactivate catalysts as they block sites and diffusion pathways [6,25–27]. In addition to deactivation, differences in the diffusivities of smaller aromatic compounds, such as benzene, toluene, and various xylenes (BTX), can contribute to selectivity trends through altering the influence of zeolite crystal morphology and Al siting during chemistries such as toluene methylation, xylene isomerization, and transalkylation [28–30]. Understanding the mass-transport of aromatics within zeolite frameworks is critical to providing insight to reaction rates, product selectivities, and catalyst deactivation.

Mass transport in zeolites involves three critical steps: adsorption to the zeolite surface, pore entrance, and intracrystalline diffusion. Macroscopic measurements of mass transport (i.e., uptake and frequency response) show that transport in small crystals (<2 μm) is primarily governed by resistance to pore entrance as evidenced by frequency response experiments examining benzene, toluene, and *para*-xylene diffusion [31] and frequency response experiments of cyclohexane diffusion through silicalite-1 [32,33]. Resistance to pore entrance can be described by pore narrowing or pore

* Corresponding author.
E-mail address: hibbitts@che.ufl.edu (D. Hibbitts).

https://doi.org/10.1016/j.micromeso.2022.111705
Received 8 October 2021; Received in revised form 17 December 2021; Accepted 12 January 2022
Available online 19 January 2022

blockage [34], for example with trace amounts of water [35]. In larger particles (>2 μm), such as those typically used for MTH chemistry, mass transport is best described by intracrystalline diffusion [31,36]. However, macroscopic techniques assume homogeneity in crystal morphology and micro-imaging has demonstrated crystals apparently identical in size and shape may exhibit different uptake rates [37]. As such, microscopic techniques, such as PFG-NMR, offer a more accurate measurement of diffusion and have similarly demonstrated that methane and n-butane diffusion are best described by intracrystalline transport barriers [38,39].

Within MFI, intracrystalline diffusion between channel intersections occurs via the straight or sinusoidal channels. Molecules can also transfer from one channel to another to diffuse in the c-direction; however, this diffusion process involves rotation of the molecule in channel intersections which occurs with high barriers for large species such as *para*-xylene [40,41] and furfuryl alcohol [42]—as such, this work focuses aromatic diffusion via the straight and sinusoidal channels without channel switching. Diffusion between channel intersections of MFI can be described as an activated jump, where a molecule must overcome an energy barrier when diffusing through straight or sinusoidal channels [38,43,44]. As such, intracrystalline diffusion can be described by an Eyring equation (Eq. (1))

$$D_{self} = D_o \times e^{-\frac{E_A}{RT}} \quad (1)$$

where D_o is an experimentally obtained pre-factor and E_A is the activation energy of diffusion. As such, transition state theory is commonly coupled with molecular dynamics simulations to examine diffusion in zeolites [45–52]. Frequency response experiments of benzene, toluene, and *para*-xylene diffusion within silicalite-1 and H-ZSM-5 (Si:Al = 45) crystals show bimodal responses [31,40,41,53], and these bimodal features are used to yield two activation barriers for diffusion. Bimodal frequencies have been interpreted as isolation of straight and sinusoidal diffusion [40,54]; however, prior work on benzene diffusion has demonstrated that the second feature only becomes apparent at benzene loadings >4 molecules per unit cell and instead interpret the bimodal response as an effect of loading [55]. As such, the validity of interpreting bimodal frequencies as straight and sinusoidal channel diffusion remains unclear. Barriers derived from bimodal frequency response experiments demonstrate that 'fast' benzene diffusion occurs with a barrier of 17 kJ mol^{-1} and the 'slow' diffusion with a barrier of 26 kJ mol^{-1}; however, as previously noted, it is unclear that these correspond to straight and sinusoidal diffusion. Diffusion via the two channel systems can be decoupled with computation techniques such as molecular dynamics (MD) simulations that suggest sinusoidal diffusion is slower for n-heptane (600 K) within MFI where straight channel diffusivities (7.2×10^{-9} m^2 s^{-1}) are higher than those of the sinusoidal channel (3.4×10^{-9} m$^{2\ s-1}$) [56]. Most experiments and computational work, however, focus on small molecules such as methane, linear alkenes, and C_6–C_8 aromatics. To our best knowledge, no DFT studies have contrasted aromatic diffusion via straight and sinusoidal channels and it remains unclear at what extent of substitution aromatic species are no longer able to diffuse via sinusoidal channels (which likely becomes diffusion limited first) and straight channels.

MFI-type zeolites are used in xylene separations and show relatively high selectivities to *para*-xylene, and this is caused, in part, by selective diffusion of *para*-xylene relative to other xylene isomers [4,29,40,57,58]. The diffusivity of a molecule can be related to its molecular size by a critical diameter, defined here as the diameter that will determine if a molecule can enter a cylindrical pore [59,60]. Typically, species with smaller critical diameters (i.e., benzene) diffuse faster than those with larger critical diameters (i.e., *meta*-xylene). For example, the diffusivity of benzene, toluene, and *para*-xylene (all with a critical diameter of 6.6 Å) through MFI is ~10^{-13} m^2 s^{-1} as reported by frequency response [61–63], zero length column (ZLC) [64,65], sorption [66], and gravimetric [67] techniques. *ortho*-Xylene and *meta*-xylene have a larger critical diameter (both with a critical diameter of 7.3 Å) and diffusivities in the range of ~10^{-16}–10^{-19} [68–71]. Experiments of aromatic diffusion through zeolites are limited to species that diffuse through crystals at reasonable time scales—generally making analysis of C_{9+} species difficult. Similarly, to our knowledge, no prior computational work has examined diffusion of bulkier aromatics through the two channels of MFI to understand which species become stuck within channel intersections.

Distortions in the framework caused by large transition states can alter reaction and diffusion barriers. Work examining alkene alkylation transition states in TON suggests that larger transition states, for example the dimerization of C_4 species via a C_8 transition state, force framework oxygen atoms to distort away from the transition state to minimize repulsive interactions [72]. These framework distortions are accompanied by an energy penalty where larger transition states are associated with larger energy penalties [72]. Framework distortions can also occur during diffusion, for example, DFT predicts that benzene diffusion through the 8-MR of CHA causes relatively small distortions in the 8MR diameter (~0.15 Å) and diffuses with a barrier of 248 kJ mol^{-1} whereas 1,2,4,5-tetramethylbenzene (durene) causes much larger distortions (0.7 Å) and diffuses with a barrier of 348 kJ mol^{-1} [73]. The qualitative interaction between critical diameters and framework distortions is clear, larger species require larger distortions, but how the tortuosity of the sinusoidal channel (as compared to the straight channel) impacts the relationships between critical diameter, framework distortion, and diffusion barriers has not been examined across a large set of methylbenzene aromatics, despite their relevance in arene methylation, transalkylation, and MTH.

This work examines diffusion barriers for benzene and all C_7–C_{12} methylbenzenes through the straight and sinusoidal channels of MFI (Silicalite-1). BTX species diffuse through the channels with relatively low barriers < 100 kJ mol^{-1} supporting that during aromatic-related chemistry these species can be formed at internal sites and then diffuse out of the framework. Other species, such as 1,2,3,4-tetraamethylbenzene may diffuse via straight channels (112 kJ mol^{-1} barrier) at reasonable timescales, but not via sinusoidal channels (189 kJ mol^{-1}), suggesting they are capable of egressing during catalysis via a 1-D pore network. However, most C_{10}–C_{12} species are essentially immobile (barriers > 150 kJ mol^{-1} for both pathways) at relevant conditions. We demonstrate that diffusion barriers trend well with the critical diameter of the molecule and that molecules with larger critical diameters cause distortions in the framework leading to higher diffusion barriers. Framework distortion is larger in the sinusoidal channel lending to sinusoidal barriers that are, on average, ~40 kJ mol^{-1} higher than straight channel diffusion barriers.

2. Methods

2.1. Density functional theory methods

The Vienna ab initio simulation package (VASP) [74–77] was used to execute DFT calculations in fully periodic MFI unit cells. All calculations were implemented in the Computational Catalysis Interface (CCI) [78]. Planewaves with an energy cutoff of 400 eV were composed using projector augmented wave (PAW) potentials. Structures were optimized using the Perdew-Burke-Ernzerhof (PBE) exchange-correlation functional [79–81] and the DFT-D3 method with Becke and Johnson damping to adjust for dispersive interactions [82–84]. Structures were optimized in a two-step process, which is ~3 × more efficient than traditional single-step optimizations [78]. In the first step, structures were electronically converged such that energies varied by < 10^{-4} eV between iterations and until the forces on each atom were < 0.05 eV Å^{-1}, and all forces were computed so using a Fast Fourier Transform (FFT) grid with a cutoff 1.5 × the planewave cutoff. In the second step, accuracy was further improved by converging to within < 10^{-6} with a FFT grid 2 × the plane-wave cutoff. No atoms were constrained during optimizations. The Brillouin Zone was sampled at the Γ-point [85].

The silicalite-1 structure (Fig. S1 in the Supplemental Information, SI) was derived from the results of van Koningsveld et al. because restructuring

artifacts are minimized in this zeolite form [86,87]. The shape and lattice parameters of silicalite-1 (a = 20.090 Å, b = 19.738 Å, c = 13.142 Å) were fixed. Previous work has demonstrated that the MFI unit cell can experience sorbate-induced restructuring at loadings as low as 1.6 molecule per unit cell (molec./u.c.) [88–90]. Here, diffusion is modeled at relatively low loadings of 1 molec./u.c. where expansion of the MFI unit cell and co-adsorbate influences on diffusion pathways and barriers may be less relevant; as such, diffusions are modeled in a single unit cell.

Structures of all methylbenzene species in the channel intersections were reoriented by rotating the structures around the a-, b-, and c-axes of the unit cell in 30°-increments, resulting in ~36 orientations attempted for each methylbenzene, as described in previous work [21]. These systematic reorientations are employed to ensure that the potential energy surface of each reactant state is sufficiently probed, while avoiding computationally expensive dynamic simulations. We note that there is no guarantee that these reorientations will identify the global minimum for a particular state; however, prior work demonstrated that these static reorientations can identify structures up to 50 kJ mol^{-1} more stable than the initial input structure [21,91]—demonstrating the importance of examining multiple structures for each state.

Diffusion pathways were modeled in a stepwise fashion using a combination of the nudged elastic band (NEB) [92] and Dimer methods [93]. NEB calculations involved 12–16 images along the pathway and were converged to 10^{-4} eV with a FFT cutoff 1.5 × the size of the plane wave cutoff. Initially, the C and H atoms in the aromatic were frozen along a fixed trajectory during the NEB and the structure of the surrounding MFI framework was optimized such that the forces on all atoms in each image were < 0.5 eV Å^{-1}. Upon convergence of this 'frozen' NEB, the NEB was re-converged to the same criteria while permitting the aromatic atoms to move. Finally, the NEB was converged so that the force on every atom was < 0.15 eV Å^{-1} and transition states searches (Dimer method) were started from these more accurate NEBs. In cases where the energy profile had multiple transition states Section 2.4, the length of the coordinate was shortened so that there was one transition state per NEB. Transition states were refined using the Dimer method [93] and optimized until the forces converged to 0.05 eV Å^{-1}, using a two-step method similar to that used for optimizations.

For each aromatic, ~12 diffusion pathways were initialized—six for straight diffusion and six for sinusoidal diffusion. Three of the six unique orientations involved changing the angle between the center of the C_6 ring and the long axis of the sinusoidal channel and each angle was investigated so that the molecule was being led by either a C-atom or a bond down the respective channel. These different reorientations only involved altering the initial orientation and the molecules were not constrained by the initial orientation. Only the orientation that resulted in the lowest energy diffusional routes will be discussed in the remainder of the manuscript.

2.2. Self-diffusivity calculation

Here, we estimate self-diffusivities of BTX species from DFT by representing diffusion of aromatics as an activated jump between channel intersections within the MFI framework. As such the diffusivity can be related back to an Eyring equation (Eq. (1)). To estimate the diffusivity of species between channel intersections, we can use the DFT-predicted energy barriers and transition state theory to estimate the D_o term, or pre-factor, of Equation (1) where prior work [73] has shown that diffusivity can be calculated by:

$$D = \lambda^2 k_1 \tag{2}$$

where λ represents the diffusion path length and k_1 can be expressed using transition state theory:

$$D = \lambda^2 \frac{k_b T}{h} e^{\frac{\Delta S_A}{R}} e^{-\frac{\Delta H_A}{RT}} \tag{3}$$

where k_b is the Boltzmann constant, h is Planck's constant, and ΔS_A and ΔH_A can be calculated from the activation potential energies (discussed in Section 3.1) and vibrational frequency analysis (see Section 2). By comparison with Eq. (1), we can see this gives a definition for pre-factor (D_o) as:

$$D_o = \lambda^2 \frac{k_b T}{h} e^{\frac{\Delta S}{R}} \tag{4}$$

Prior work in SSZ-13 using DFT to estimate diffusion barriers through the 8-membered ring of CHA demonstrate that diffusivities calculated by Eq. (4) generally agree well with those predicted by kinetic Monte Carlo simulations [73], suggesting this approach is sufficient for estimating diffusivities within MFI.

3. Results and discussion

3.1. General trends in aromatic diffusion

3.1.1. Straight channel potential energy surfaces

Diffusion between intersections via the straight channel of MFI involves passing through two adjacent 10-membered rings (MRs) with a diameter of ~5.6 Å. Potential energy surfaces are constructed from NEB calculations converged to forces of 0.15 eV Å^{-1} to better understand the diffusion pathway of each molecule via the straight channel. The potential energy surfaces shown here reflect the orientations leading to the lowest energy diffusion barriers (of the 6 attempted, described in Section 2.2). Fig. 1a shows the potential energy surface of benzene referenced to the energy of benzene adsorbed in the channel intersection in its most favorable orientation. As benzene traverses the straight channel, there are three local maxima before reaching the next channel intersection. For each NEB-local maxima, transition states are isolated with Dimer calculations yielding barriers 2–10 kJ mol^{-1} lower than those estimated by the NEB (Fig. 1). We attribute the energy differences to differences in convergence criteria for wavefunctions and atomic forces between the NEB and Dimer methods. The vertical lines on Fig. 1 represent the point on the potential energy surface when the center of the benzene ring passes the 10-MRs of the straight channel. Both 10-MRs have an associated transition state where benzene is either entering (Fig. 1d) or leaving (Fig. 1f) the straight channel and these occur with potential energy barriers (ΔE_0) of 11 and 15 kJ mol^{-1}. There is a third transition state corresponding to benzene passing between the two 10-MRs (Fig. 1e) with a ΔE_0 of 12 kJ mol^{-1}. We can measure a relative distance between the center of the benzene ring and the center of the two 10-MRs (defined by the 10 Si atoms) to quantify the positions of the transition state relative to the 10-MRs (transition states close to 0 are 'entering' the straight channel and transition states close to 1 are 'exiting' the straight channel). The three transition states of benzene diffusion occur at 0.01, 0.54, and 1.07 (Fig. 1)—confirming they represent entering, traversing, and exiting the straight channel. Similar to benzene, the potential energy surfaces of toluene and *para*-xylene (Fig. 1b–c) exhibit three similarly sized maxima corresponding to entering (Fig. 1g,j), traversing (Fig. 1h,k), and exiting the straight channel (Fig. 1i,l). The converged transition states of benzene, toluene, and *para*-xylene straight channel diffusion fall within 4 kJ mol^{-1}, suggesting they diffuse with barriers within the error of these DFT methods. Toluene and *para*-xylene have additional methyl substituents; however, the molecules orient in such a way that limits interactions between these methyl groups and surrounding framework causing diffusion to occur with nearly identical barriers.

Larger species have methyl-substituents that interact with the zeolite framework in a manner that alters the shape of the potential energy surface and increases diffusion barriers. In the remaining potential energy surfaces, again reflecting the optimal diffusion pathway of ~6 orientations examined, we observe a variety of surface shapes including, 1) a single large transition state, 2) two asymmetric peaks, 3) three transition states with two higher energy ones nearly and one smaller peak, and 4) four transition states with two small peaks and two large

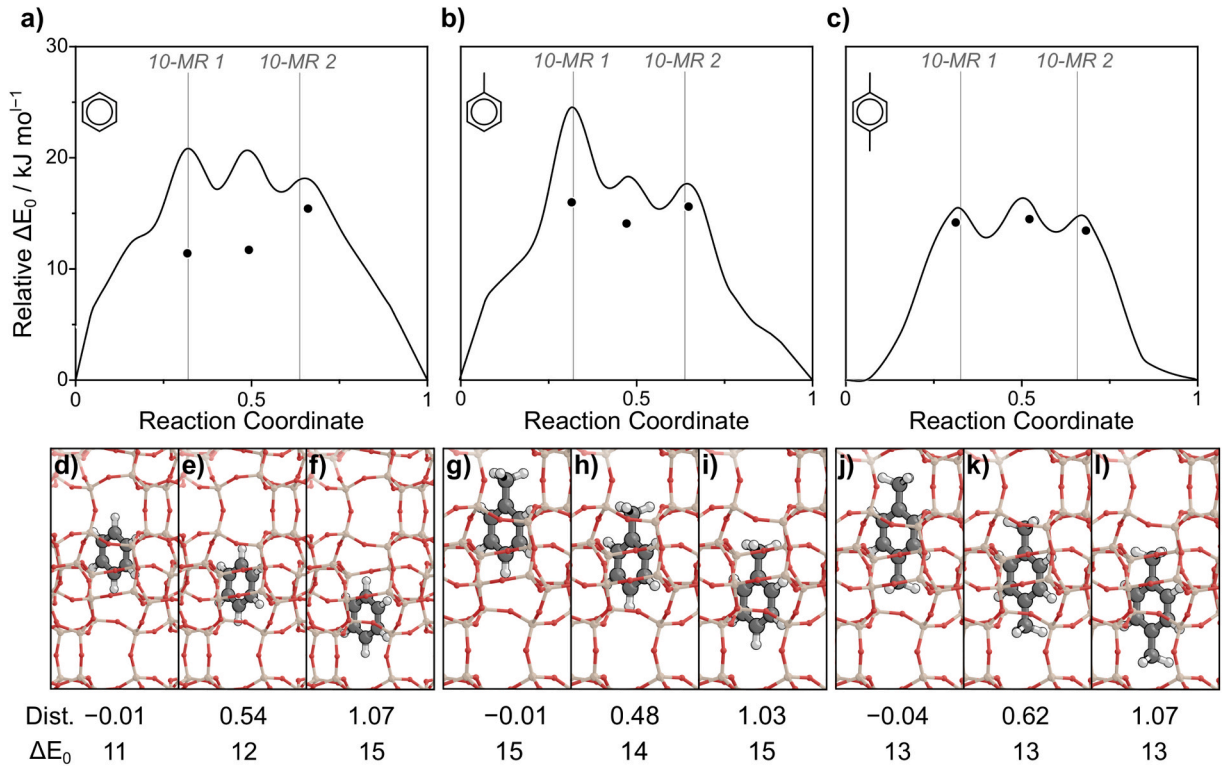

Fig. 1. Potential energy surface of benzene straight channel diffusion (NEB method, converged to within 0.15 eV $Å^{-1}$) for a) benzene, b) toluene, and c) *para*-xylene. Dots are the energies of converged transition states (Dimer method, converged to within 0.05 eV $Å^{-1}$). Lines represent benzene crossing the 10 membered rings of the straight channel. Images of each transition state are shown in d–l. Potential energies are reported in kJ mol^{-1}.

peaks. The first category is well demonstrated by the most favorable *ortho*-xylene potential energy surface with a single large transition state when the center of the aromatic is between the two 10-MRs (Fig. 2a). There is a small shoulder feature as the aromatic enters and exits the 10-MRs; however, the largest ΔE_0, 37 kJ mol^{-1}, occurs when the structure is fully within the straight channel where interaction with the surrounding framework is maximized (Fig. 2e) with a relative distance of 0.79 between the two 10-MRs. Similar to *ortho*-xylene, the most favorable potential energy surface of 1,2,4-trimethylbenzene, 1,2,3,4-tetramethylbenzene, and 1,2,4,5-tetramethylbenzene all show a single transition state (Fig. 2b–d) where the center of the ring is between the two 10-MRs and methyl-substituents are interacting with one or both of the 10-MRs (Fig. 2f–h). Generally these transition states occur when the center of the ring is closer to the second 10-MR ranging from a relative distance of 0.75–0.89 along the straight channel.

Other methylbenzenes diffuse through the straight channels with two asymmetric transition states. For example, *meta*-xylene diffusion has one transition state associated with entering the straight channel with a ΔE_0 of 24 kJ mol^{-1} (relative distance of −0.03, where the center of the ring has not passed the center of the 10 MR) and a second when the molecule is between the two 10-MRs (relative distance of 0.67) with a ΔE_0 of 40 kJ mol^{-1} (Fig. 3a). Similarly, the pentamethylbenzene potential energy surface has two disproportionately sized peaks associated with methyl substituents are interacting with both 10-MRs (ΔE_0 of 199 kJ mol^{-1}) and the aromatic exiting the second 10-MR (115 kJ mol^{-1}) (Fig. 3). In both cases, the highest energy transition state involves methyl-substituents interacting with both 10-MRs. Notably, these potential energy surfaces are not symmetric, which may be attributed to asymmetry in the molecule itself and in the distortions to the 10-MRs as the molecule traverses the straight channel.

The third category is well demonstrated by 1,2,3-trimethylbenzene, 1,3,5-trimethylbenzene and 1,2,3,5-tetramethylbenzene, each of which have three peaks on the potential energy surface (Fig. 4) associated with entering the 10-MR, traversing the channel, and exiting the 10-MR. 1,3,5-trimethylbenzene and 1,2,3,5-tetramethylbenzene have a smaller peak associated with ring structure entering the straight channel (ΔE_0 of 136 and 122 kJ mol^{-1}, respectively), while the two meta methyl-substituents remain mostly in the channel intersection. The two larger peaks are associated with methyl-substituents interacting with the two 10-MRs while diffusing down the straight channel (occurring with ΔE_0 of 185–190 kJ mol^{-1}, Table 1). Conversely, the two large peaks of 1,2,3-trimethylbenzene (ΔE_0 of 103 and 106 kJ mol^{-1}) are associated with a methyl substituent oriented directly towards either 10-MR while the smaller barrier is associated with the ring structure exiting the second 10-MR (estimated at 77 kJ mol^{-1}). Overall, the transition states of bulkier aromatics species generally occur where the center of the C_6 ring is within the straight channel and the methyl substituents are interacting with the 10-MRs.

Finally, the potential energy surface of hexamethylbenzene has two large peaks in the middle and two smaller peaks at the beginning and end (Fig. 5). Here, the two smaller peaks correspond to the methyl substituents entering (ΔE_0 of 166 kJ mol^{-1}) and exiting (ΔE_0 of 167 kJ mol^{-1}) the straight channel before the center of the ring has entered the channel system. The two larger peaks at 0.24 and 0.74 (Fig. 5) occur with nearly identical barriers (ΔE_0 of 244 kJ mol^{-1} and 243 kJ mol^{-1}) and are associated with the aromatic traversing the straight channel. Notably, the potential energy surface of hexamethylbenzene is remarkably symmetric, possibly because the symmetry of the molecule results in symmetric distortions of the straight channel as the ring passes.

Despite different potential energy surfaces, the orientation of the aromatic relative to the long-axis of the straight channel is consistent for all examined aromatics (Fig. 6). Three different orientations were initiated for straight channel diffusion based on the orientation of the ring to the axis of the straight channel (45°, 67.5°, and 90°), and in all cases the most favorable orientation of diffusion involved the ring being oriented along the longest axis of the unit cell (~43°, Fig. 6). Initial orientations were also started where either a methyl-substituent (or H)

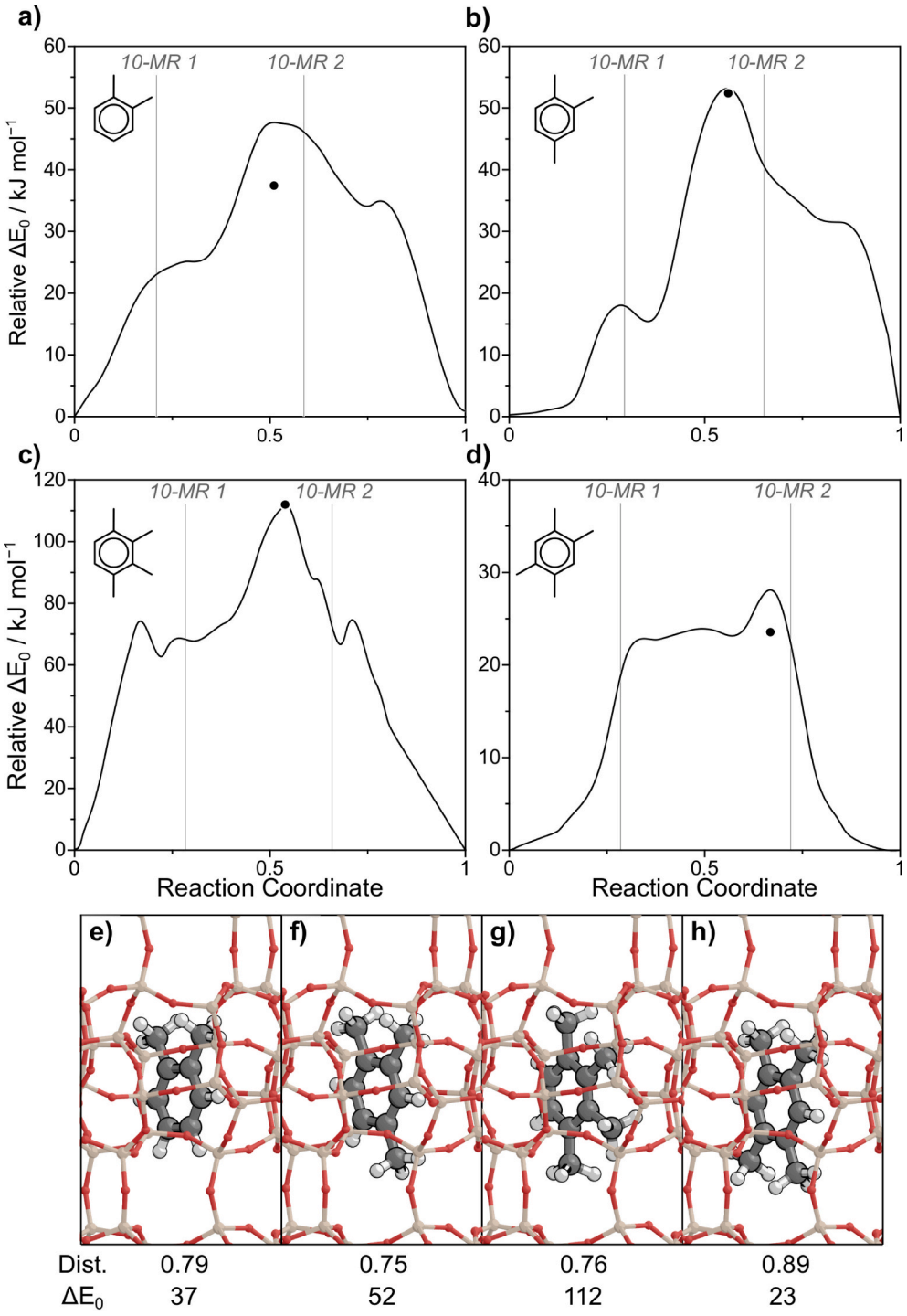

Fig. 2. Potential energy surfaces of a) 1,2-dimethylbenzene, b) 1,2,4-trimethylbenzene, c) 1,2,3,4-tetramethylbenzene, and d) 1,2,4,5-tetramethylbenzene diffusing down the straight channel. Images of each transition state are shown in parts e–f. The relative distance of the transition state and potential energy of the transition states (kJ mol^{-1}) are also reported. Scales in parts a-d vary to emphasize the shape of the potential energy surfaces.

or C–C bond was oriented down the b-axis. For example, 1,2-dimethylbenzene diffuses down with a C–C bond oriented along the b-axis (Fig. 6). Conversely, 1,3,5-trimethylbenzene orients so that a methyl-substituent is oriented down the b-axis. Generally, we find the preferred orientation down the b-axis varies between molecules based on the position of methyl-substituents on the ring and that molecules tend to orient so that interaction between methyl-substituents and the surrounding framework is minimized.

Potential energy of straight channel diffusion surfaces show that the diffusion can be considered a multi-step process (in most cases) and, generally, we find that the potential energy surface between two channel intersections is not symmetric—possibly because distortions in the framework and ring structure change as the rings traverse the straight channel. Many species display multiple peaks associated with diffusion, however, the high-energies of the intermediate states (within the channel) suggest that these interstitial sites can be neglected in most cases for estimating diffusion rates. These pathways are thus treated (using transition state theory) as having a single effective barrier that matches the highest barrier

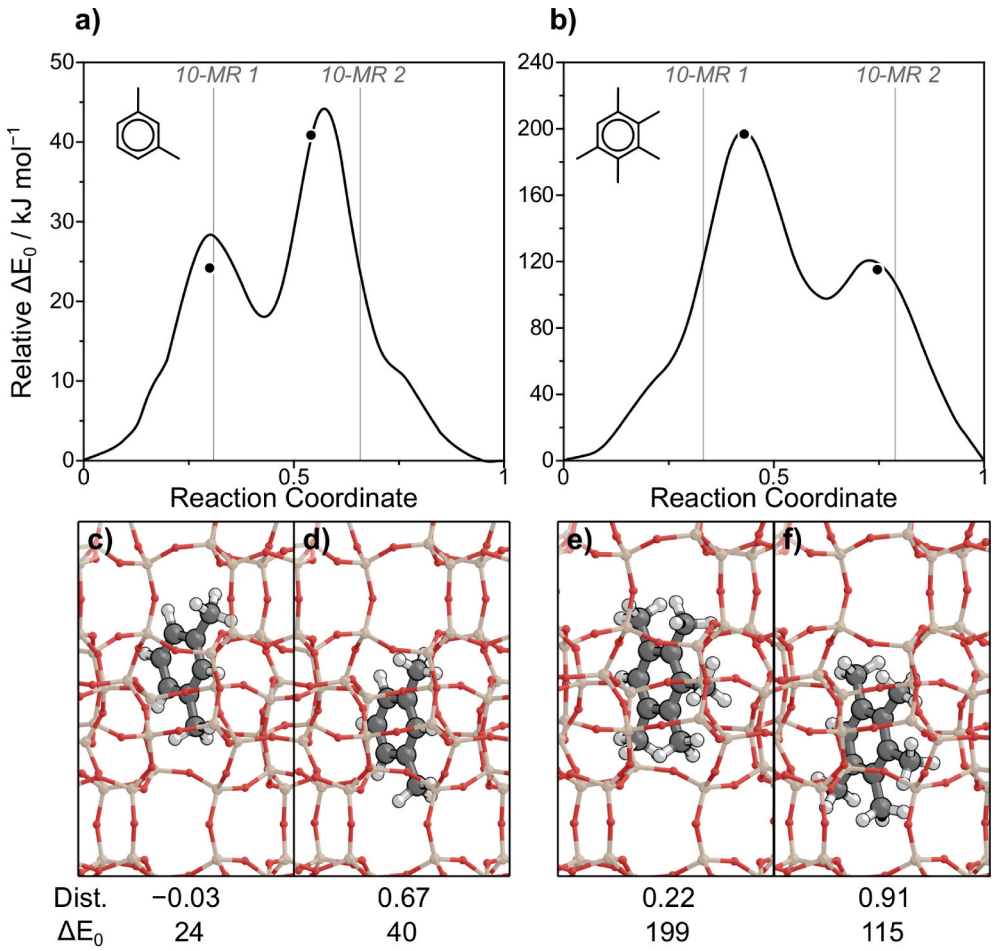

Fig. 3. Potential energy surface of a) *meta*-xylene and b) pentamethylbenzene with associated figures of each transition state in parts c–f. The relative distance of the transition state and potential energy of the transition states (kJ mol^{-1}) are also reported. Scales in parts a-b vary to emphasize the shape of the potential energy surfaces.

along the multi-step pathway, as done in similar work investigating diffusion through the 8-MR of CHA [73].

3.1.2. Sinusoidal channel potential energy surfaces

The sinusoidal channel, similar to the straight channel, consists of two 10-MRs. However, the sinusoidal channel is more tortuous than the straight channel, so molecules must rotate and distort during diffusion. Similar to Section 3.1.1, we examine the potential energy surface of C_6–C_{12} aromatics traversing through the sinusoidal channel. Starting with the simplest molecule, benzene, the potential energy surface has two large peaks—corresponding to benzene entering (ΔE_0 of 52 kJ mol^{-1}, Fig. 7a) and exiting the sinusoidal channel (ΔE_0 of 23 kJ mol^{-1}, Fig. 7a). These barriers reflect the most favorable orientation of benzene diffusion when the center of the ring is perpendicular to the b-axis (Fig. 6). Similar to the straight channel, we can compare the center of the aromatic ring and the 10-MRs of the sinusoidal channel to estimate the location of each transition state along the sinusoidal channel, where a value of 0 corresponds to benzene passing the center of the first 10-MR and a value of 1 corresponds to benzene passing the second 10-MR. The two benzene transition states occur at a value of 0, where benzene enters the sinusoidal channel, and 0.99, where benzene exits the sinusoidal channel (Fig. 6). Similarly, the potential energy surfaces of toluene (Fig. 7b) and *para*-xylene (Fig. 7c) also show two peaks corresponding to entering and exiting the 10-MRs of the sinusoidal channel. Sinusoidal diffusion barriers of toluene and *para*-xylene (56 kJ mol^{-1} and 50 kJ mol^{-1}, respectively) are within 6 kJ mol^{-1} of benzene suggesting DFT cannot accurately predict differences in diffusion rates between these three molecules.

Additional methyl substituents confound the potential energy surfaces of sinusoidal channel diffusion, which typically have multiple barriers corresponding to interactions with the 10-MRs and distortions and rotations of the molecule and its methyl substituents along the sinusoidal path. Potential energy surfaces and associated transition state structures for 1,2,3-trimethylbenzene, 1,2,4,5-tetramethylbenzene, and pentamethylbenzene are shown in Fig. 8 to demonstrate the complexity of sinusoidal diffusion. The potential energy surfaces of all species are shown in Section S3 of the SI. The path of 1,2,3-trimethylbenzene shows at least four transition states (Fig. 8a) associated with entering the 10-MR (105 kJ mol^{-1}, Fig. 8d), traversing the sinusoidal channel (131 kJ mol^{-1}, Fig. 8e), rotation of the molecule (110 kJ mol^{-1}, Fig. 8f), and exiting the second 10-MR into the channel intersection (99 kJ mol^{-1}, Fig. 8g). Similarly, the potential energy surface of pentamethylbenzene shows at least four transition states associated with entering the channel (132 kJ mol^{-1}), interacting with the 10-MRs (260 and 282 kJ mol^{-1}), and exiting the sinusoidal channel (147 kJ mol^{-1}, Fig. 7c, i–k). Conversely, 1,2,4,5-tetramethylbenzene has a single transition with a ΔE_0 of 70 kJ mol^{-1} associated with methyl substituents interacting with both 10-MRs positioned at 0.73 along the path of the sinusoidal channel (Fig. 8h). Generally, the diffusion of these species results in notable distortions of both the ring structure and the framework, which likely contributes to their higher barriers and is further discussed in Section 3.1.3.

3.1.3. General trends in diffusion

Both straight and sinusoidal diffusion barriers are examined here, and in all cases we find that straight channel barriers are lower, by an

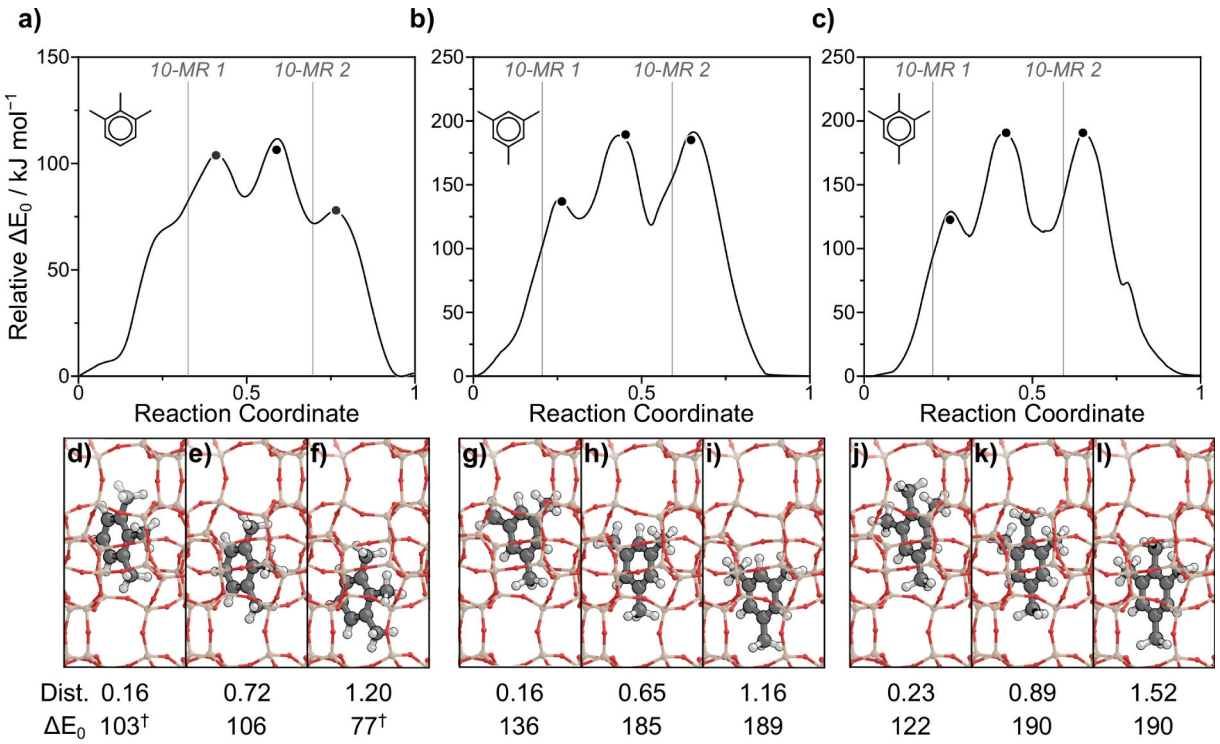

Fig. 4. Potential energy surface of a) 1,2,3-trimethylbenzene, b) 1,3,5-trimethylbenzene, and c) 1,2,3,5-tetramethylbenzene with associated figures of each transition state parts d–l. The relative distance of the transition state and potential energy of the transition states (kJ mol^{-1}) are also reported. Scales in parts a-c vary to emphasize the shape of the potential energy surfaces. The † symbol refers to transition states estimated from the potential energy surface.

average of 39 kJ mol^{-1}, than sinusoidal diffusion barriers. Diffusion via both channels involves traversing two 10-MRs, but the tortuous nature of the sinusoidal channel forces both the molecule and channel to distort more, compared to the straight channel, to accommodate the diffusion. Here, we examine the effects that additional methyl-substituents have on diffusion barriers through examining the size of the molecule, distortion of the framework, and distortion of the diffusing aromatic—all of which play a role in diffusion barriers.

Generally, diffusion barriers increase as the extent of methyl-substitution around the aromatic increases; however, the barriers are better described by the specific position of the methyl substituents on the ring through the critical diameters [59,60]. For example, *ortho*- and *para*-xylene both have 2 methyl substituents (C_8 rings) but the diffusion barriers are ~30 kJ mol^{-1} lower for *para*-xylene, because the position of methyl-substituents in *para*-xylene allows for minimal interaction with the surrounding framework compared to *ortho*-xylene. Fig. 9a shows the groupings of molecules along their critical diameters which range from 6.6 Å to 9.1 Å, reported in previous work [59,60]. Species with the smallest critical diameter, 6.6 Å, diffuse with the lowest ΔE_0 barriers via the straight and sinusoidal channels ranging from 13 to 15 kJ mol^{-1} for straight channel and 50–56 kJ mol^{-1} for sinusoidal channel. As the critical diameter increases to 9.1 Å, the average barrier also increases in each grouping thus confirming that critical diameter is an important metric in diffusion barriers and species with larger critical diameters tend to have larger diffusion barriers.

During diffusion, aromatic rings distort as they diffuse through the straight and sinusoidal channels and these distortions increase diffusion barriers. We measure the distortion in each aromatic by taking a 3N-dimension distance between the atoms of the C_6 ring in the transition state (with methyl-substituents removed) to the corresponding C_6 ring optimized in the gas phase. Benzene diffusion down the straight channel results in small ring distortions (0.05 Å), while diffusion via the sinusoidal channel results in slightly larger ring distortions (0.06 Å)—likely because of the slightly smaller pore diameter of the sinusoidal channel coupled with the more tortuous path. Rings with larger critical diameters tend to experience more distortion as they diffuse through MFI, which contributes to higher diffusion barriers (Fig. 9b). For example, 1,2,3-trimethylbenzene diffusion via the straight and sinusoidal channels results in a 0.31 Å and 0.43 Å distortion in the C_6 ring, respectively (Table S1).

As methylbenzenes traverse the 10-MRs of the straight and sinusoidal channels, the framework must also distort to accommodate the large methyl substituents. Here, we quantify the degree of framework distortion by calculating a 3N-dimensional distance (Section S5 of the SI) between the Si-form framework structure with and without an optimized diffusion transition state—the 3N-dimensional distance reported here is meant to qualitatively relate an extent of lattice distortion to diffusion barrier. The diffusion barriers trend well with the magnitude of deviation in 3N-dimensional distance where species that distort the framework more have higher diffusion barriers (Fig. 10). For example, benzene straight channel diffusion (ΔE_0 of 15 kJ mol^{-1}) causes a minimal framework distortion of 0.38 Å whereas hexamethylbenzene straight channel diffusion (ΔE_0 of 244 kJ mol^{-1}) distorts the framework 4.97 Å. Similarly, sinusoidal barriers generally trend well with framework distortion (Fig. 10), but generally involve a higher degree of framework distortion compared to the straight channel, which partially contributes to the higher barriers. For example, toluene diffusion via the straight channel changes the 3N-dimensional distance by 0.93 Å while diffusion via the sinusoidal channel distorts the framework by 1.43 Å. On average, the framework is distorted 2.6 × more via the sinusoidal channel than the straight channel leading to sinusoidal diffusion barriers that are, on average, 2.2 × higher. These data show that multiple factors govern diffusion barriers in MFI including distortion of the aromatic ring and the framework and that the relationship of these distortions to straight and sinusoidal diffusion is different; as such, the relationship between the barrier and framework distortion is not a single value function.

Table 1
Reported diffusivities of BTX diffusion through H-ZSM-5 and Silicalite-1 (Si:Al = ∞) Crystals.

Ref	Si: Al[a]	Method[b]	Temp. *K*	ΔH *kJ mol^{-1}*	Diffusivity *m^2 s^{-1}*
benzene					
This Work	∞	DFT	373	13,[c] 52[d]	1.7×10^{-11}[c], 3.5×10^{-17}[d]
Bülow et al. [63]	135	FR	423	28	1×10^{-13}
Gobin et al. [40]	45	FR	343	17,[c] 26[d]	4.95×10^{-13}[c], 5.1×10^{-14}[d]
Song et al. [55]	∞	FR	303	–	1.46×10^{-12}[c], 5.2×10^{-14}[d]
Song et al. [32]	∞	FR	348	–	1×10^{-13}
Shen et al. [61]	∞	FR	375	–	1.14×10^{-13}
Van-Den-Begin et al. [94]	∞	FR	388	25	1×10^{-13}
Eic et al. [64]	∞	ZLC	373	27	1.54×10^{-13}
Ruthven et al. [68]	∞	ZLC	348	27	1.8×10^{-13}
Zikanova et al. [67]	135	Uptake	363	26	7×10^{-13}
Heering et al. [66]	35	Uptake	313	–	2.5×10^{-14}
Doelle et al. [95]	34	Uptake	313	–	1.5×10^{-13}
Wu et al. [69]	∞	Uptake	373	21	5.6×10^{-15}
Zikanova et al. [67]	∞	Uptake	363	18	2.5×10^{-12}
Jobic et al. [96]	∞	Neutron Spin	465	30	1.3×10^{-14}
Rungsirisaku et al. [46]	∞	MD	300	–	2.5×10^{-10}
Foreseter et al. [97]	∞	MD	300	27,[c] 34[d]	5.4×10^{-14}[c], 3.6×10^{-14}[d]
Kolokathis et al. [98]	∞	MD	300	–	2.5×10^{-13}[c], 8.67×10^{-14}[d]
Snurr et al. [99]	∞	IRC	300	37,[c] 38[d]	1×10^{-16}
toluene					
This Work	∞	DFT	373	14,[c] 56[d]	2.3×10^{-12}[c], 1.9×10^{-18}[d]
Gobin et al. [40]	45	FR	343	19,[c] 27[d]	4.01×10^{-13}[c], 4.0×10^{-14}[d]
Song et al. [32]	∞	FR	348	–	4.7×10^{-13}[c], 5.4×10^{-14}[d]
Muller et al. [100]	∞	Uptake	320	–	3.9×10^{-14}
Choudhary et al. [70]	39.7	Uptake	308	36	7.9×10^{-16}
***ortho*-xylene**					
This Work	∞	DFT	373	43,[c] 89[d]	1.1×10^{-16}[c], 1.1×10^{-23}[d]
Ruthven et al. [68]	∞	ZLC	373	33	3.6×10^{-14}
Wu et al. [69]	∞	Uptake	293	–	2.2×10^{-16}
Choudhary et al. [70]	39.7	Uptake	308	36	9×10^{-18}
Mirth et al. [71]	35.5	Uptake	373	30	6.5 × 10−18
***meta*-xylene**					
This Work	∞	DFT	373	40,[c] 71[d]	5.1×10^{-17}[c], 4.5×10^{-21}[d]
Choudhary et al. [70]	39.7	Uptake	308	38	3×10^{-19}
Mirth et al. [71]	35.5	Uptake	373	29	7×10^{-19}
Doelle et al. [95]	34	Uptake	313	–	2.4×10^{-14}
Wu et al. [69]	∞	Uptake	293	–	4.1×10^{-16}
Yang et al. [101]	47	AIMD	670	23,[c] 47[d]	–
***para*-xylene**					
This Work	∞	DFT	373	13,[c] 49[d]	6.5×10^{-12}[c], 7.7×10^{-19}[d]
Gobin et al. [40]	45	FR	343	20,[c] 27[d]	3.9×10^{-13}[c], 1.7×10^{-14}[d]
Song et al. [32]	∞	FR	348	–	8.2×10^{-13}
Ruthven et al. [68]	∞	ZLC	373	30	4.1×10^{-13}
Choudhary et al. [70]	39.7	Uptake	308	18	5.13×10^{-16}
Mirth et al. [71]	35.5	Uptake	373	–	6×10^{-16}
Wu et al. [69]	∞	Uptake	293	15	3.1×10^{-15}
Yang et al. [101]	47	AIMD	670	19,[c] 16[d]	–

[a] A Si:Al ratio of ∞ corresponds to silicalite-1.
[b] Methods include molecular dynamics (MD, forcefield based), frequency response (FR), zero-length column (ZLC), internal reaction coordinate (IRC).
[c] Values reported for 'fast' diffusion process.
[d] Values reported for 'slow' diffusion process.

3.2. Benzene, toluene, and xylene diffusivities

Prior literature has focused on understanding diffusion barriers and diffusivities of benzene, toluene, and xylenes (BTX)—partly because the time scale of BTX diffusion allows for experimental measurements. Table 1 summarizes literature diffusivities and diffusion barriers for BTX species using a combination of experimental and theoretical techniques in both silicalite-1 and H-ZSM-5 materials. The enthalpic barriers (ΔH) calculated here represent diffusion in a perfect crystal whereas experimental studies can be subject to convoluting factors including pore-mouth effects, loading effects, and heterogeneity in crystal morphology. Despite this, the DFT-calculated ΔH values (373 K) for benzene diffusion via the straight channel (14 kJ mol^{-1}) agree well with literature reported values (17–37 kJ mol^{-1}) as shown in Table 1 [40,67,69,70]. Similarly, DFT-calculated straight channel diffusion enthalpy barriers of toluene (14 kJ mol^{-1}), *ortho*-xylene (43 kJ mol^{-1}), *meta*-xylene (40 kJ mol^{-1}), and *para*-xylene (13 kJ mol^{-1}) are in close agreement to the values previously reported by literature (Table 1). As

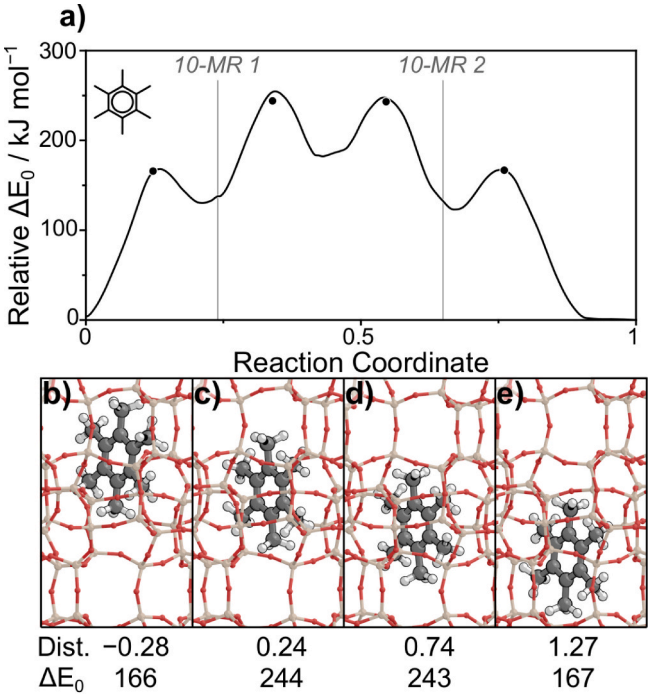

Fig. 5. a) Potential energy surface of hexamethylbenzene with associated figures of each transition state parts b–e. The relative distance of the transition state and potential energy of the transition states (kJ mol^{-1}) are also reported.

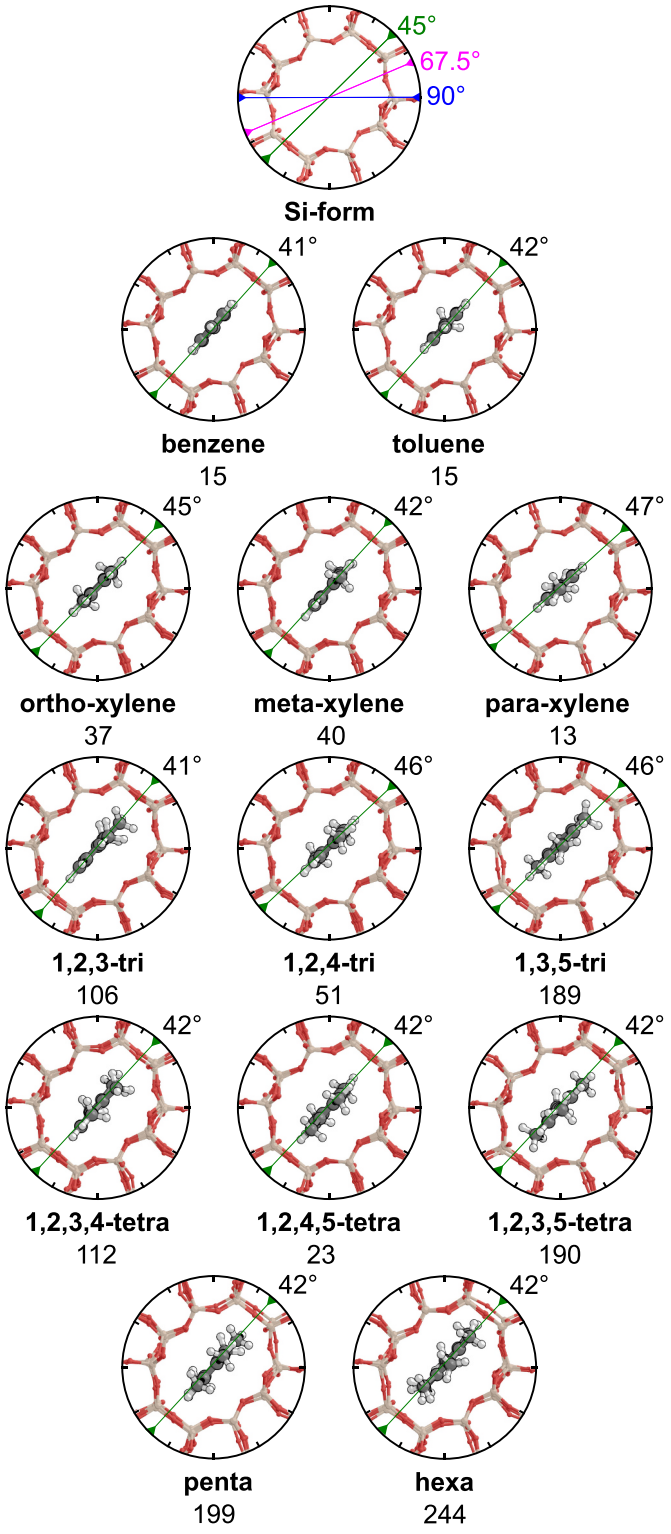

Fig. 6. Preferred orientation of the highest energy straight channel diffusion transition state for C_6–C_{12} methylbenzenes. The orientation relative to 0° are reported. Potential energy barriers (ΔE_0) of each transition state are reported in kJ mol^{-1}.

discussed in Section 3.1, DFT-calculated barriers of straight channel diffusion for benzene, toluene, and *para*-xylene are within 4 kJ mol^{-1} of one another, as these species have the same kinetic diameter, while *ortho*- and *meta*-xylene (critical diameter of 7.3 Å) have barriers 20 kJ mol^{-1} higher as the additional methyls are forced to interact with the surrounding framework.

While BTX straight channel diffusion barriers are well-predicted by our DFT methods, we find that DFT-calculated sinusoidal channel diffusion barriers are much higher than those representing 'slow' diffusion from bimodal frequency response experiments (Table 1). For example, the DFT-calculated enthalpy barrier of benzene diffusion via the sinusoidal channel is 52 kJ mol^{-1} while frequency response experiments yield a 'slow' diffusion barrier of 26 kJ mol^{-1} (Table 1). To ensure the difference in barriers are not caused by spurious errors in DFT methods, benzene diffusion in a 1 × 2 × 1 supercell was tested to ensure that propagation of framework distortion was not artificially increasing barriers. Sinusoidal diffusion within the supercell occurred with ΔE_0 of 50 kJ mol^{-1} (Fig. S2)—suggesting that the error does not stem from periodic effects. Benzene diffusion was also examined in a second MFI framework structure (based on Olson et al.) [102], and the sinusoidal diffusion in this MFI framework model occurred with a barrier of 50 kJ mol^{-1} (Fig. S3)—nearly identical to the 52 kJ mol^{-1} barrier in the MFI model derived from van Koningsveld (used throughout this work). As previously mentioned, bimodal frequencies can represent a 'fast' and 'slow' diffusion process; however, the cause of these different diffusion modes is unclear. Prior work has suggested bimodal frequencies represent straight and sinusoidal diffusion modes [40,54] while others have suggested it is a consequence of loading where benzene adsorption in silicalite-1 show a single diffusion mode at loadings lower than 4 molec./u.c. but two diffusion modes at higher loadings [55]. Additional causes for different diffusivities can be attributed to the presence of Brønsted acid sites, where metadynamic simulations have shown that Brønsted acid sites within zeolites lower ethene and propene diffusion barriers by ~20 kJ mol^{-1} through the 8-MR of SAPO-34 [103], and work comparing benzene diffusion in Silicalite-1 and ZSM-5 find diffusivities that are 3 × higher in Silicalite-1 (Table 1) [67]. It is also possible that bimodal responses can reflect differences in crystal topology where the presence of intergrowths and silanol defects can lead to multiple diffusion processes. Therefore, we suggest that the bimodal responses observed in H-ZSM-5 crystals do not represent straight and sinusoidal diffusion and are more likely caused by distinct straight-channel diffusion pathways that are influenced by crystal loading, the proximity of Brønsted acid sites, and/or silanol defect groups.

Experimental diffusion studies typically report diffusivities rather than barriers, and Table 1 summarizes some of the past work examining BTX diffusion through H-ZSM-5 or silicalite-1. A wide range of diffusivities are reported in literature; for example, measured benzene diffusivities range from 10^{-16} to 10^{-12} m^2 s^{-1}, and those for para-xylene range from 10^{-16} to 10^{-11} m^2 s^{-1}. Most techniques listed in Table 1 reflect diffusivity measured by macroscopic techniques, and the large ranges are likely, in part, related to the measurement technique. As previously mentioned, heterogeneity in crystal morphology, even within the same batch, can lead to substantial differences in observed diffusivity—motivating the use of microscopic techniques to quantify diffusivities more accurately through zeolite crystals [104,105]. The wide range of experimentally observed diffusivities can also be attributed to defects in the crystal (intergrowths or mesopores) [106], the presence of surface barriers [57,104,107], acid site density [103,108,109], and loading [88–90]. The magnitude of these ranges reflects the difficulty in comparing measured and computed values. Here, we estimate self-diffusivities of BTX species from DFT by representing diffusion of aromatics as an activated jump between channel intersections within the MFI framework. As such, the diffusivity can be related back to an Eyring equation (Eq. (1)). Straight channel barriers for BTX are predicted well by theory; however, self-diffusivities calculated by Eq. (4) (Section 2.2) using DFT-predicted ΔS_A and ΔH_A do not match the range of reported experimental values (Table 1). Benzene self-diffusivities down the straight channel and sinusoidal channels (373 K) are 2.1 × 10^{-9} m^2 s^{-1} and 4.4 × 10^{-15} m^2 s^{-1} (373 K), whereas literature values range between 10^{-16} to 10^{-12} m^2 s^{-1}. Despite the large range of experimentally measured benzene diffusivities, these unadjusted DFT-derived values

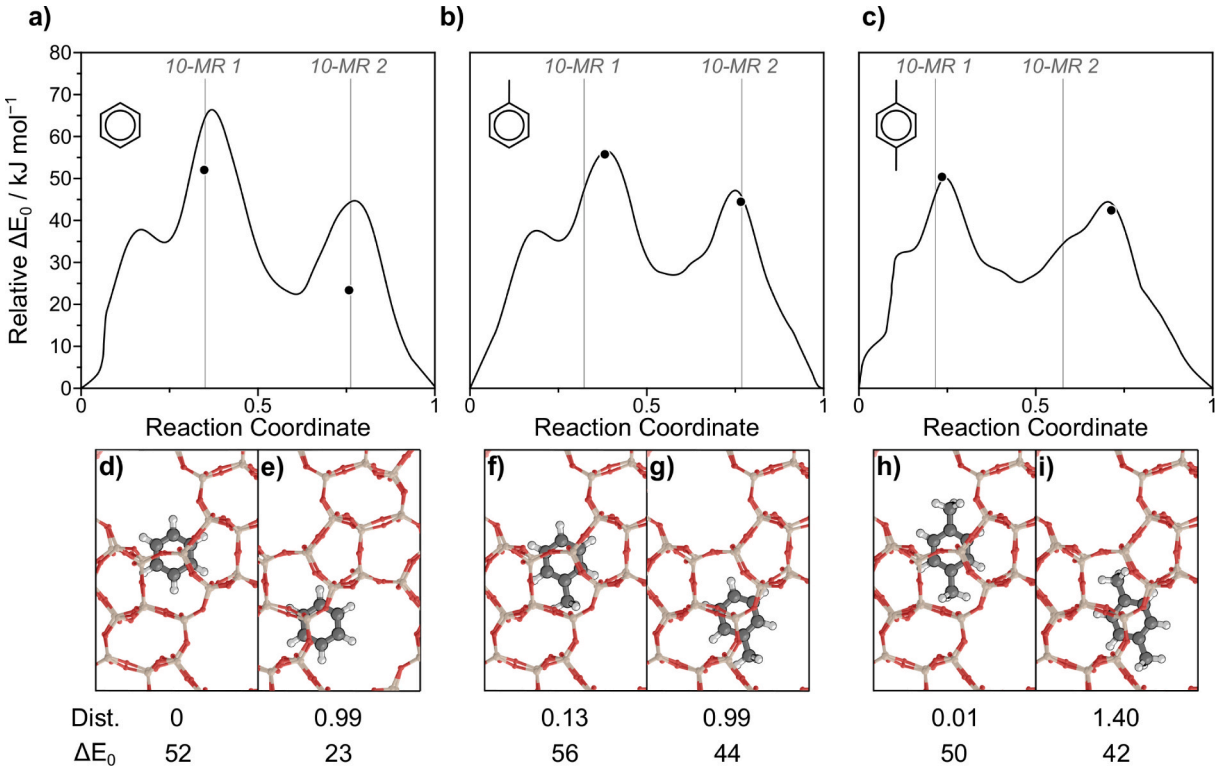

Fig. 7. Potential energy surfaces of a) benzene, b) toluene, and c) *para*-xylene sinusoidal diffusion with associated figures of each transition state parts d–i. The relative distance of the transition state and potential energy of the transition states (kJ mol^{-1}) are also reported.

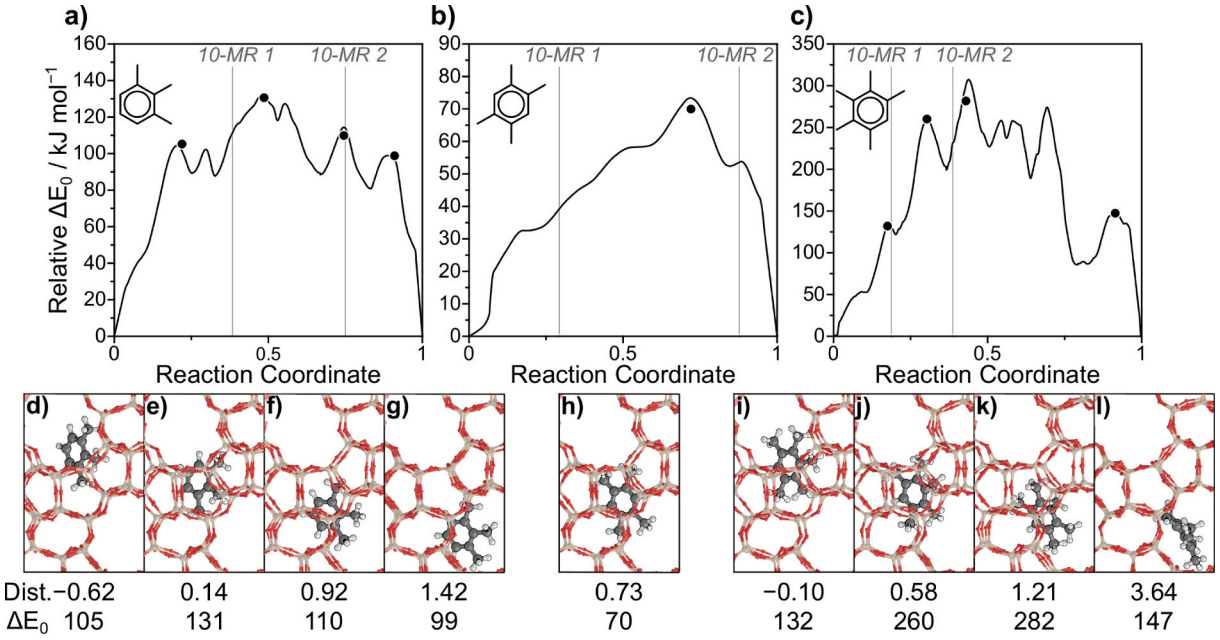

Fig. 8. Potential energy surfaces of a) 1,2,3-trimethylbenzene, b) 1,2,4,5-tetramethylbenzene (durene), and c) pentamethylbenzene sinusoidal diffusion with associated figures of each transition state parts d–l. Scales in parts a-c vary to emphasize the shape of the potential energy surfaces. The relative distance of the transition state and potential energy of the transition states (kJ mol^{-1}) are also reported. Potential energy surfaces for all species are shown in Section S3 of the Supplemental Information.

miss the range entirely. Frequency response experiments of benzene in H-ZSM-5 (Si:Al = 45), specifically, measure a 'fast' diffusion process with a diffusivity of 8.0×10^{-13} m^2 s^{-1} [40], different by ~3 orders of magnitude from the DFT estimate (2.1×10^{-9} m^2 s^{-1}), despite activation barriers calculated by DFT and estimated by frequency response being within 4 kJ mol^{-1}. Comparison of DFT-calculated and experimentally obtained pre-factors (D_o, dependent on entropy shown in Eq. (5)) shows that the straight and sinusoidal DFT-calculated D_o terms (1.7×10^{-7} m^2 s^{-1} and 7.9×10^{-8} m^2 s^{-1}) are significantly overestimated compared to experiments (1.9×10^{-10} m^2 s^{-1} and 4.5×10^{-10})—

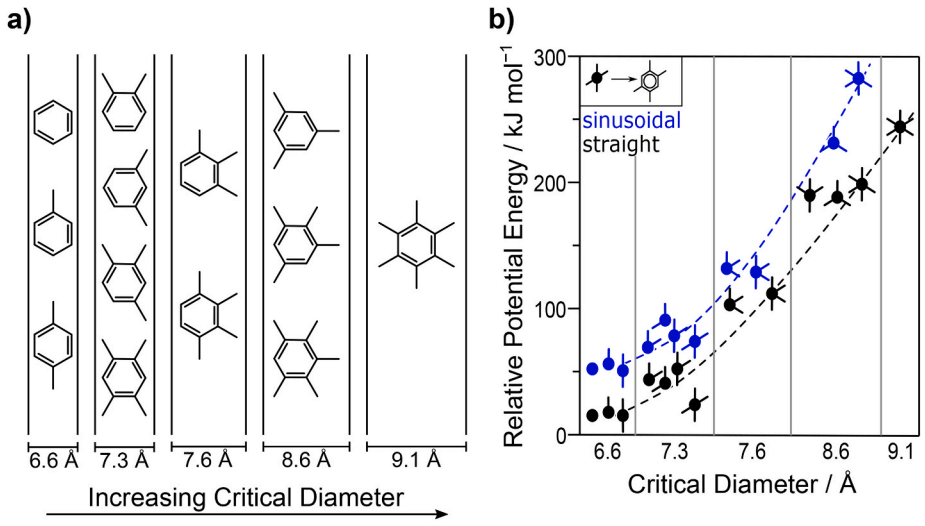

Fig. 9. a) Groupings of species based on critical diameter, and b) activation energy of diffusion via the straight (blue) and sinusoidal (black) channels grouped by their effective radii. Symbols in (b) depict the location of methyl substituents (see inset) and their x-positions are shifted to avoid overlap. Lines are to guide the eye. (For interpretation of the references to colour in this figure legend, the reader is referred to the Web version of this article.)

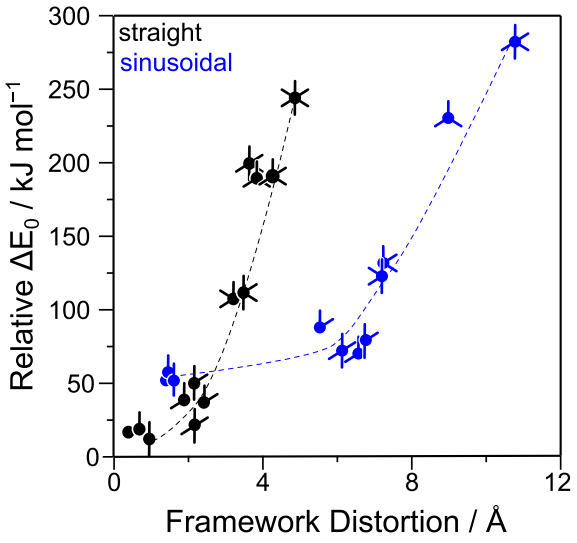

Fig. 10. Potential energy barriers (kJ mol^{-1}, relative to respective adsorbed aromatic) of straight (black) and sinusoidal (blue) diffusion barriers shown as the extent of framework distortion (3N-dimensional distance) increases. The extent of framework distortion is reported in Table S1. (For interpretation of the references to colour in this figure legend, the reader is referred to the Web version of this article.)

suggesting that the error stems from the entropy terms in Eq. (4). The activation entropy (ΔS_A) predicted by DFT is −33 J mol^{-1} K^{-1}, and this was calculated using the harmonic oscillator approximation and vibrational frequencies for adsorbed benzene and the dominant transition state mediating straight-channel diffusion (Fig. 1f). Harmonic oscillator approximations, however, have been shown to significantly underestimate adsorbate entropies within zeolites [110–114], owing to the non-harmonic nature of frustrated translations and rotations that appear as low-frequency vibrations in fixed displacement normal mode analysis. From this harmonic oscillator approach, the DFT-predicted ΔS_{ads} of benzene (−134 J mol^{-1} K^{-1}) is 54 J mol^{-1} K^{-1} more negative than those measured by experiments (−80 J mol^{-1} K^{-1}) [115,116], further suggesting that the error stems from an underestimation of the entropy of adsorbed aromatics in the intersection. Instead of using harmonic oscillator approximations, here, we also estimate the entropy of adsorbed aromatics through a recent correlation developed by examining the adsorption of linear C_3–C_9 hydrocarbons in a variety of zeolite frameworks:

$$\Delta S_{ads} = \left(S_{2D,\ trans} + F_{rot} S_{1D,\ rot} + S_{vib}\right) - S_{gas} \quad (5)$$

where the adsorption entropy is estimated by assuming that molecules will lose one degree of translational freedom ($S_{2D,trans}$) and a fraction of their rotational degrees of freedom (F_{rot}) dependent on the cavity diameter of the framework—molecules in smaller frameworks will be more hindered and lose more rotational degrees of freedom compared to larger frameworks [117]. Using Eq. (5) to correct the entropy of adsorbed benzene, the ΔS_{ads} becomes −94 J mol^{-1} K^{-1} which is within 15 J mol^{-1} K^{-1} of the experimentally predicted value (Fig. 11). For the transition states, no such correction is applied (Fig. 11), because the transition state has no translational degrees of freedom and the rotational modes are heavily restricted by the straight channel. This is demonstrated in Fig. 11 showing that the entropy of activation (ΔS_A) changes from −33 kJ mol^{-1} (uncorrected) to −73 kJ mol^{-1} by adjusting the entropy of adsorbed benzene, and that this estimated ΔS_A agrees well with that estimated from sorption and diffusion experiments (−88 kJ mol^{-1}).

Straight channel diffusivities calculated using corrected entropies for adsorbed benzene, toluene, and *para*-xylene, are on the order of 10^{-11}–10^{-12} and are slightly higher than the average diffusivity reported in Table 1. However, the difference in diffusivities can be attributed to a <10 kJ mol^{-1} underestimation in diffusion barrier which falls within the error of DFT. Conversely, the DFT-predicted diffusivities of *ortho*- and *meta*-xylene are slightly lower than those predicted by experiments, but this can similarly be attributed to slight overestimation of the diffusion barriers (Table 1). Differences between DFT-calculated and measured diffusivities are well within the error of DFT methods and, as previously mentioned, may also be attributed to differences in loading, Al content, crystal size, skin effects, and intracrystalline defects.

3.3. Diffusivities and barriers of all species

Self-diffusivities of each aromatic (Table 2) are calculated using the DFT-predicted diffusion barriers and Equation (4) using estimated adsorption entropies (Eq. (5)) as described above. These barriers and self diffusivities are calculated in a perfect MFI crystal and do not account for

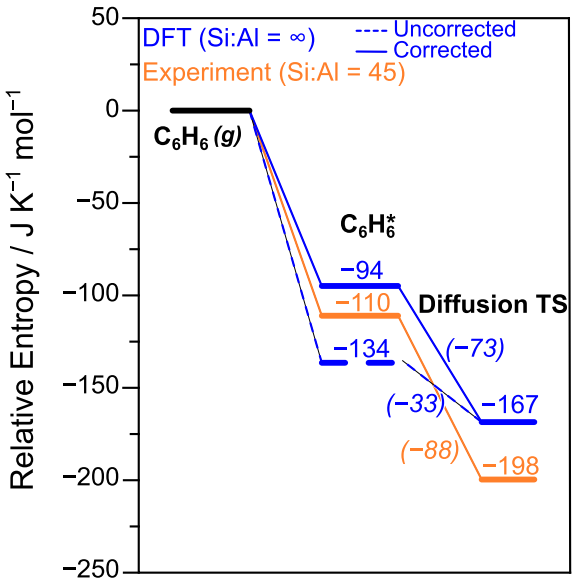

Fig. 11. Relative entropy (J K^{-1} mol^{-1}) of adsorption of benzene into the channel intersection as calculated by sorption experiments from Pope et al. (Si:Al unreported, 323 K) combined with entropy estimate of benzene straight channel diffusion as measured by frequency response experiments in H-ZSM-5 (Gobin et al., Si:Al = 45, 373 K, using Eq. (4) to solve for entropy). Blue lines depict DFT-calculated (373 K) benzene adsorption and diffusion using uncorrected (dashed) and corrected (solid) entropy values. (For interpretation of the references to colour in this figure legend, the reader is referred to the Web version of this article.)

the effects loading, defects, or aluminum content; however, they do offer estimates of diffusivities not measurable by current experimental techniques. From the values reported in Table 2, we can predict which species will be capable of diffusing through the straight and sinusoidal channels during reaction. While making these predictions, it is important to note that these diffusion barrier ranges are just reference points, the balance between mass transport and kinetic limitations will depend on the rate constants of the relevant kinetic processes. Here, we are considering barriers of ~100 kJ mol^{-1} to represent 'facile' diffusion, and this value is chosen based on commonly reported barriers for reaction involving aromatics including arene methylation [19,21,118], aromatic disproportionation [11], and methanol-to-olefins [16,119,120] which generally range from 150 to 200 kJ mol^{-1}.

BTX species, 1,2,4-trimethylbenzene, and 1,2,4,5-tetramethylbenzene diffuse via the straight and sinusoidal channels with ΔE_0 barriers ≤74 kJ mol^{-1}, suggesting that these species can diffuse via both channels during reaction (depending on the kinetics governing the reaction). These species have a critical diameter less than 7.3 Å and cause minimal distortions in the framework as they diffuse through the channel systems, resulting in the low barriers and facile diffusion. 1,2,3-trimethylbenzene and 1,2,3,4-tetramethylbenzene diffuse through the straight and sinusoidal channels with ΔE_0 of ≤112 and ≤131 kJ mol^{-1}, respectively—suggesting these species may experience MFI as a pseudo-1D zeolite framework where transport is only possible via the straight channel. Finally, species with a kinetic diameter larger than 8.6 Å including 1,3,5-trimethylbenzene, 1,2,3,5-tetramethylbenzene, pentamethylbenzene, and hexamethylbenzene diffuse through both channels with barriers >190 kJ mol^{-1} suggesting that, once formed, these species will likely become 'stuck' within the intersections of MFI and contribute to deactivation. Again, we stress that these categories and a cutoff of 100 kJ mol^{-1} are dependent on competition between mass transport and kinetics and can change for different reactions and that these barriers and diffusivities are merely reference points. However, we believe it is important to report and categorize these DFT-predicted barriers of aromatic diffusion, particularly because such understanding of aromatic diffusion is critical to understanding competition between mass transport and kinetics but not reportable by current experimental techniques.

4. Conclusions

This work uses periodic DFT calculations to examine diffusion of benzene and all twelve C_7–C_{12} methylbenzene species via the straight and sinusoidal channels of silicalite-1 (Si-form of MFI). Molecules within the channels of silicalite-1 orient so that methyl-substituents minimally interact with the surrounding framework to lower diffusion barriers. Barriers via both channels increase as the critical diameter (a diameter corresponding to a compact orientation along the pore) increases, and diffusion barriers via the straight channel are predicted to be significantly lower (by an average of 40 kJ mol^{-1}) than via the more tortuous sinusoidal channel. Benzene, toluene, and para-xylene—species with the smallest critical diameters—diffuse via the straight channel with barriers of 13–15 kJ mol^{-1} and sinusoidal channel with barriers 52–56 kJ mol^{-1}. BTX species as well as 1,2,4-trimethylbenzene, and 1,2,4,5-tetramethylbenzene all diffuse via the straight and sinusoidal channels with barriers <100 kJ mol^{-1}, suggesting 'facile' diffusion (relatively speaking) in either channel. Bulkier species, such as 1,3,5-trimethylbenzene, 1,2,3,5-tetramethylbenzene, as well as penta- and hexamethylbenzene have barriers via either channel >150 kJ mol^{-1}, suggesting

Table 2
Barriers and corrected diffusivities of straight and sinusoidal diffusion for all methylbenzenes.

Species	ΔE_0		Diffusivity		Category
	Str	Sin	Str	Sin	
	kJ mol^{-1}	kJ mol^{-1}	m^2 s^{-1}	m^2 s^{-1}	
Benzene	15	52	1.7×10^{-11}	3.5×10^{-17}	str + sin
Toluene	15	56	2.7×10^{-12}	1.9×10^{-18}	str + sin
ortho-Xylene	37	88	1.1×10^{-16}	1.1×10^{-23}	str + sin
meta-Xylene	40	71	5.1×10^{-17}	4.5×10^{-21}	str + sin
para-Xylene	13	50	6.5×10^{-12}	7.7×10^{-19}	str + sin
1,2,3-trimethylbenzene	106	131	8.8×10^{-27}	8.5×10^{-31}	str only
1,2,4-trimethylbenzene	51	74	7.0×10^{-20}	4.8×10^{-23}	str + sin
1,3,5-trimethylbenzene	189	231	6.0×10^{-40}	6.2×10^{-46}	site blocking
1,2,3,4-tetramethylbenzene	112	121	3.0×10^{-28}	4.0×10^{-30}	str only
1,2,3,5-tetramethylbenzene	190	–	2.6×10^{-40}	–	site blocking
1,2,4,5-tetramethylbenzene	23	70	3.1×10^{-15}	1.8×10^{-22}	str + sin
pentamethylbenzene	199	282	3.2×10^{-42}	1.0×10^{-52}	site blocking
hexamethylbenzene	244	–	6.0×10^{-49}	–	site blocking

[†]Represents a diffusion barrier estimated from converged NEBs but all attempts at Dimers were unsuccessful. Potential energy surfaces are reported in Section S3 of the Supplemental Information.

these species are effectively immobile within zeolites and that if they are formed by intracrystalline reactions they can generally be considered trapped, and only capable of productive chemistry via isomerization and cracking reactions. It is likely that these larger molecules, once formed, also contribute to deactivation during aromatics-related chemistry as they can block sites, restrict the diffusion of other molecules, and can act as precursors to polyaromatic species.

During diffusion, the framework must distort, especially with larger aromatics, to accommodate the transition state passing through the straight and sinusoidal channels. Here, we show that this distortion correlates to activation barriers. For example, benzene diffusion via the straight channel (potential energy barrier of 15 kJ mol^{-1}) distorts the framework by 0.38 Å whereas pentamethylbenzene straight channel diffusion (potential energy barrier of 199 kJ mol^{-1}) distorts the framework by 3.64 Å. Furthermore, species cause larger distortions when diffusing down the more tortuous sinusoidal channel compared to the straight channel. Para-xylene straight channel diffusion (potential energy barrier of 15 kJ mol^{-1}) distorts the framework by 0.97 Å and sinusoidal diffusion (potential energy barrier of 50 kJ mol^{-1}) causes a 1.57 Å distortion. On average, diffusion via the sinusoidal channel causes framework distortions that are larger, by a factor of ~2.6 ×, than those via the straight channel, despite both being composed of a pair of 10-MR structures. This greater extent of framework distortion, and larger barriers (by ~38 kJ mol^{-1}), were also seen for sinusoidal diffusion in other MFI framework structures (derived from different crystallographic information files) and was also observed in diffusion pathway calculations within supercell calculations that spatially separate diffusion events in the periodic DFT models. While DFT-predicted barriers for straight-channel diffusion are in good agreement with measured values for BTX species, there is a large discrepancy between predicted barriers via the sinusoidal channel and those derived from the 'slow' diffusion process of bimodal frequency response measurements for BTX species. These discrepancies cast doubt on the interpretation of the bimodal response in the experiments as straight and sinusoidal diffusion processes.

Self-diffusivities can be estimated from DFT-calculated diffusion barriers using transition state theory. The entropies of adsorbed states (C_6H_6*) are under-estimated by DFT, leading to under-estimated entropy losses upon activation (ΔS_A) and thus prefactors and diffusivities that are over-estimated by a factor of 10–1000 for straight channel diffusion of BTX species, despite those diffusion barriers being in close agreement with measured values. Here, we show these entropic errors can be overcome using recently developed correlations for adsorbate entropies that suggest that adsorbates lose 1° of translation and 1.28° of rotational freedom [117] upon adsorption in MFI. For BTX species, we find that the DFT-predicted straight channel diffusivities are ~10^{-13} m^2s^{-1} and are the same order of magnitude of those predicted by frequency response experiments.

While critical factors, such as the role of Al sites, crystalline defects, and intermolecular interactions still need to be considered, this data gives insights into the role of methyl substitution (and thus critical diameter), framework distortion, path tortuosity, and entropy estimates in the intracrystalline diffusion barriers and diffusivities of a wide range of aromatic molecules in the ubiquitous MFI framework.

CRediT authorship contribution statement

Mykela DeLuca: Data curation, Formal analysis, Methodology, Writing – original draft. **David Hibbitts:** Writing – review & editing, Supervision, Resources, Project administration, Investigation, Funding acquisition.

Declaration of competing interest

The authors declare that they have no known competing financial interests or personal relationships that could have appeared to influence the work reported in this paper.

Acknowledgements

We thank Dr. Sergey Vasenkov (University of Florida) for technical discussion and advice regarding this study. This work was funded by NSF CAREER Award (1942684-CBET). Computational resources were provided by the Extreme Science and Engineering Discovery Environment (XSEDE) and University of Florida Research Computing.

Appendix A. Supplementary data

Supplementary data to this article can be found online at https://doi.org/10.1016/j.micromeso.2022.111705.

References

[1] L. Young, J. Catal. 76 (1982) 418.
[2] S. Mesa, J. Arboleda, A. Echavarría, F.E. López-Suárez, Chem. Eng. Sci. 208 (2019) 115147.
[3] D. Mitsuyoshi, K. Kuroiwa, Y. Kataoka, T. Nakagawa, M. Kosaka, K. Nakamura, S. Suganuma, Y. Araki, N. Katada, Microporous Mesoporous Mater. 242 (2017) 118.
[4] W. Kaeding, J. Catal. 69 (1981) 392.
[5] N.R. Meshram, S.G. Hegde, S.B. Kulkarni, Zeolites 6 (1986) 434.
[6] J.-C. Kim, K. Cho, S. Lee, R. Ryoo, Catal. Today 243 (2015) 103.
[7] S. Zheng, A. Jentys, J. Lercher, J. Catal. 241 (2006) 304.
[8] F. Llopis, G. Sastre, A. Corma, J. Catal. 227 (2004) 227.
[9] F. Bauer, W.-H. Chen, H. Ernst, S.-J. Huang, A. Freyer, S.-B. Liu, Microporous Mesoporous Mater. 72 (2004) 81.
[10] C. Fernandez, I. Stan, J.-P. Gilson, K. Thomas, A. Vicente, A. Bonilla, J. Pérez-Ramírez, Chem. Eur J. 16 (2010) 6224.
[11] Y. Byun, D. Jo, D.N. Shin, S.B. Hong, ACS Catal. 4 (2014) 1764.
[12] I. Yarulina, S. Bailleul, A. Pustovarenko, J.R. Martinez, K.D. Wispelaere, J. Hajek, B.M. Weckhuysen, K. Houben, M. Baldus, V. Van Speybroeck, F. Kapteijn, J. Gascon, ChemCatChem 8 (2016) 3057.
[13] C.-M. Wang, Y.-D. Wang, Y.-J. Du, G. Yang, Z.-K. Xie, Catal. Sci. Technol. 5 (2015) 4354.
[14] S. Ilias, R. Khare, A. Malek, A. Bhan, J. Catal. 303 (2013) 135.
[15] M. Zhang, S. Xu, Y. Wei, J. Li, J. Wang, W. Zhang, S. Gao, Z. Liu, Chin. J. Catal. 37 (2016) 1413.
[16] B. Arstad, J.B. Nicholas, J.F. Haw, J. Am. Chem. Soc. 126 (2004) 2991.
[17] C. Baerlocher, L.B. McCusker, (2013).
[18] S. Wang, Y. Chen, Z. Wei, Z. Qin, T. Liang, M. Dong, J. Li, W. Fan, J. Wang, J. Phys. Chem. C 120 (2016) 27964.
[19] S. Svelle, M. Visur, U. Olsbye, S. Saepurahman, M. Bjørgen, Top. Catal. 54 (2011) 897.
[20] I. Hill, A. Malek, A. Bhan, ACS Catal. 3 (2013) 1992.
[21] M. DeLuca, P. Kravchenko, A. Hoffman, D. Hibbitts, ACS Catal. 9 (2019) 6444.
[22] D. Lesthaeghe, A. Horré, M. Waroquier, G.B. Marin, V. Van Speybroeck, Chem. Eur J. 15 (2009) 10803.
[23] C.-M. Wang, Y.-D. Wang, Z.-K. Xie, Z.-P. Liu, J. Phys. Chem. C 113 (2009) 4584.
[24] K. De Wispelaere, K. Hemelsoet, M. Waroquier, V. Van Speybroeck, J. Catal. 305 (2013) 76.
[25] A. Hwang, A. Bhan, Acc. Chem. Res. 52 (2019) 2647.
[26] K. Lee, S. Lee, Y. Jun, M. Choi, J. Catal. 347 (2017) 222.
[27] D. Rojo-Gama, M. Signorile, F. Bonino, S. Bordiga, U. Olsbye, K.P. Lillerud, P. Beato, S. Svelle, J. Catal. 351 (2017) 33.
[28] J.H. Ahn, R. Kolvenbach, O.Y. Gutiérrez, S.S. Al-Khattaf, A. Jentys, J.A. Lercher, Microporous Mesoporous Mater. 210 (2015) 52.
[29] K. Beschmann, L. Riekert, J. Catal. 141 (1993) 548.
[30] G. Noh, M.L. Sarazen, J. Catal. 404 (2021) 679–689.
[31] O.C. Gobin, S.J. Reitmeier, A. Jentys, J.A. Lercher, J. Phys. Chem. C 113 (2009) 20435.
[32] L. Song, L.V.C. Rees, Microporous Mesoporous Mater. 35–36 (2000) 301.
[33] L. Gueudré, E. Jolimaître, N. Bats, W. Dong, Adsorption 16 (2010) 17.
[34] A.R. Teixeira, C.-C. Chang, T. Coogan, R. Kendall, W. Fan, P.J. Dauenhauer, J. Phys. Chem. C 117 (2013) 25545.
[35] D. Tzoulaki, W. Schmidt, U. Wilczok, J. Kärger, Microporous Mesoporous Mater. 110 (2008) 72.
[36] A.R. Teixeira, X. Qi, C.-C. Chang, W. Fan, W.C. Conner, P.J. Dauenhauer, J. Phys. Chem. C 118 (2014) 22166.
[37] J.C. Saint Remi, A. Lauerer, C. Chmelik, I. Vandendael, H. Terryn, G.V. Baron, J.F. M. Denayer, J. Kärger, Nat. Mater. 15 (2016) 401.
[38] S. Vasenkov, W. Böhlmann, P. Galvosas, O. Geier, H. Liu, J. Kärger, J. Phys. Chem. B 105 (2001) 5922.
[39] S. Vasenkov, J. Kärger, Microporous Mesoporous Mater. 55 (2002) 139.
[40] O.C. Gobin, S.J. Reitmeier, A. Jentys, J.A. Lercher, Microporous Mesoporous Mater. 125 (2009) 3.
[41] L. Song, Z.-L. Sun, L.V.C. Rees, Microporous Mesoporous Mater. 55 (2002) 31.

[42] D. Fu, J.J.E. Maris, K. Stanciakova, N. Nikolopoulos, O. van der Heijden, L.D. B. Mandemaker, M.E. Siemons, D.S. Pastene, L.C. Kapitein, F.T. Rabouw, F. Meirer, B. Weckhuysen, Angew Chem. Int. Ed. Engl. 134 (5) (2021) e202114388.
[43] J. Kärger, H. Pfeifer, R. Haberlandt, J. Chem. Soc., Faraday Trans. 1 76 (1980) 1569.
[44] J. Xiao, J. Wei, Chem. Eng. Sci. 47 (1992) 1123.
[45] D. Dubbeldam, E. Beerdsen, T.J.H. Vlugt, B. Smit, J. Chem. Phys. 122 (2005) 224712.
[46] R. Rungsirisakun, T. Nanok, M. Probst, J. Limtrakul, J. Mol. Graph. Model. 24 (2006) 373.
[47] E.J. Maginn, A.T. Bell, D.N. Theodorou, J. Phys. Chem. 100 (1996) 7155.
[48] D. Dubbeldam, E. Beerdsen, S. Calero, B. Smit, J. Phys. Chem. B 110 (2006) 3164.
[49] J.S. Camp, D.S. Sholl, J. Phys. Chem. C 120 (2016) 1110.
[50] A.F. Voter, J.D. Doll, J. Chem. Phys. 82 (1985) 80.
[51] T. Mosell, G. Schrimpf, J. Brickmann, J. Phys. Chem. 100 (1996) 4582.
[52] C. Tunca, D.M. Ford, J. Chem. Phys. 111 (1999) 2751.
[53] D. Shen, L.V.C. Rees, Faraday Trans. 91 (1995) 2027.
[54] D. Shen, L.V. Rees, Zeolites 11 (1991) 684.
[55] L. Song, Z.-L. Sun, H.-Y. Ban, M. Dai, L.V.C. Rees, Phys. Chem. Chem. Phys. 6 (2004) 4722.
[56] E.B. Webb, G.S. Grest, M. Mondello, J. Phys. Chem. B 103 (1999) 4949.
[57] M. Baumgärtl, A. Jentys, J.A. Lercher, J. Phys. Chem. C 123 (2018) 8092.
[58] K. Miyake, Y. Hirota, K. Ono, Y. Uchida, S. Tanaka, N. Nishiyama, J. Catal. 342 (2016) 63.
[59] C.E. Webster, R.S. Drago, M.C. Zerner, J. Phys. Chem. B 103 (1999) 1242.
[60] C.E. Webster, R.S. Drago, M.C. Zerner, J. Am. Chem. Soc. 120 (1998) 5509.
[61] D. Shen, L.V.C. Rees, Zeolites 11 (1991) 666.
[62] D. Shen, L.V.C. Rees, Faraday Trans. 89 (1993) 1063.
[63] M. Bülow, H. Schlodder, L.V.C. Rees, R.E. Richards, In:, new developments in zeolite science and technology, in: Proceedings of the 7th International Zeolite Conference, Elsevier, 1986, pp. 579–586.
[64] M. Eic, D.M. Ruthven, In:, zeolites: facts, figures, future Part A, in: Proceedings of the 8th International Zeolite Conference, Elsevier, 1989, pp. 897–905.
[65] S. Brandani, M. Jama, D. Ruthven, Microporous Mesoporous Mater. 35–36 (2000) 283.
[66] J. Heering, M. Kotter, L. Reikert, Chem. Eng. Sci. 37 (1982) 581.
[67] A. Zikánová, M. Bülow, H. Schlodder, Zeolites 7 (1987) 115.
[68] D.M. Ruthven, M. Eic, E. Richard, Zeolites 11 (1991) 647.
[69] P. Wu, A. Debebe, Y.H. Ma, Zeolites 3 (1983) 118.
[70] V.R. Choudhary, V.S. Nayak, T.V. Choudhary, Ind. Eng. Chem. Res. 36 (1997) 1812.
[71] G. Mirth, J. Cejka, J.A. Lercher, J. Catal. 139 (1993) 24.
[72] M.L. Sarazen, E. Iglesia, ChemCatChem 10 (2018) 4028.
[73] A.T. Smith, P.N. Plessow, F. Studt, Chem. Phys. 541 (2021) 111033.
[74] G. Kresse, J. Hafner, Phys. Rev. B 47 (1993) 558.
[75] G. Kresse, J. Hafner, Phys. Rev. B 49 (1994) 14251.
[76] G. Kresse, J. Furthmüller, Phys. Rev. B 54 (1996) 11169.
[77] G. Kresse, J. Furthmüller, Comput. Mater. Sci. 6 (1996) 15.
[78] P. Kravchenko, C. Plaisance, D. Hibbitts, Published as pre-print on, https://chemrxiv.org/articles/preprint/8040737, 2019.
[79] J.P. Perdew, K. Burke, M. Ernzerhof, Phys. Rev. Lett. 77 (1996) 3865.
[80] Y. Zhang, W. Yang, Phys. Rev. Lett. 80 (1998) 890.
[81] B. Hammer, L.B. Hansen, J.K. Nørskov, Phys. Rev. B 59 (1999) 7413.
[82] S. Grimme, S. Ehrlich, L. Goerigk, J. Comput. Chem. 32 (2011) 1456.
[83] H. Schröder, A. Creon, T. Schwabe, J. Chem. Theor. Comput. 11 (2015) 3163.
[84] S. Grimme, J. Antony, S. Ehrlich, H. Krieg, J. Chem. Phys. 132 (2010) 154104.
[85] H.J. Monkhorst, J.D. Pack, Phys. Rev. B 13 (1976) 5188.
[86] A. Hoffman, M. DeLuca, D. Hibbitts, J. Phys. Chem. C 123 (2019) 6572.
[87] H. van Koningsveld, Acta Crystallogr. B Struct. Sci. 46 (1990) 731.
[88] C.A. Fyfe, G.J. Kennedy, C.T. De Schutter, G.T. Kokotailo, J. Chem. Soc., Chem. Commun. (1984) 541.
[89] C.A. Fyfe, H. Strobl, G.T. Kokotailo, G.J. Kennedy, G.E. Barlow, J. Am. Chem. Soc. 110 (1988) 3373.
[90] H. van Koningsveld, F. Tuinstra, H. van Bekkum, J.C. Jansen, Acta Crystallogr. B Struct. Sci. 45 (1989) 423.
[91] M. DeLuca, C. Janes, D. Hibbitts, ACS Catal. 10 (2020) 4593.
[92] H. Jónsson, G. Mills, K.W. Jacobsen, B.J. Berne, G. Ciccotti, in: D.F. Coker (Ed.), Classical and Quantum Dynamics in Condensed Phase Simulations, World Scientific, 1998, pp. 385–404.
[93] G. Henkelman, H. Jónsson, J. Chem. Phys. 111 (1999) 7010.
[94] N. Van-Den-Begin, L.V.C. Rees, J. Caro, M. Bülow, Zeolites 9 (1989) 287.
[95] H. Doelle, J. Catal. 71 (1981) 27.
[96] H. Jobic, M. Bée, S. Pouget, J. Phys. Chem. B 104 (2000) 7130.
[97] T.R. Forester, W. Smith, Faraday Trans. 93 (1997) 3249.
[98] P.D. Kolokathis, E. Pantatosaki, C.-A. Gatsiou, H. Jobic, G.K. Papadopoulos, D. N. Theodorou, Mol. Simulat. 40 (2014) 80.
[99] R.Q. Snurr, A.T. Bell, D.N. Theodorou, J. Phys. Chem. 98 (1994) 11948.
[100] G. Muller, T. Narbeshuber, G. Mirth, J.A. Lercher, J. Phys. Chem. 98 (1994) 7436.
[101] Q. Chen, J. Liu, B. Yang, Nat. Commun. 12 (2021) 3725.
[102] D.H. Olson, G.T. Kokotailo, S.L. Lawton, W.M. Meier, J. Phys. Chem. 85 (1981) 2238.
[103] P. Cnudde, R. Demuynck, S. Vandenbrande, M. Waroquier, G. Sastre, V. Van Speybroeck, J. Am. Chem. Soc. 142 (13) (2020) 6007–6017.
[104] L. Karwacki, M.H.F. Kox, D.A.M. de Winter, M.R. Drury, J.D. Meeldijk, E. Stavitski, W. Schmidt, M. Mertens, P. Cubillas, N. John, A. Chan, N. Kahn, S. R. Bare, M. Anderson, J. Kornatowski, B.M. Weckhuysen, Nat. Mater. 8 (2009) 959.
[105] J.T.C. Wennmacher, T. Li, C. Zaubitzer, M. Gemmi, E. Mugnaioli, T. Gruene, J. A. van Bokhoven, Microporous Mesoporous Mater. 294 (2020) 109897.
[106] H.I. Adawi, F.O. Odigie, M.L. Sarazen, Mol. Syst. Des. Eng. 6 (2021) 903–917.
[107] G. Sastre, J. Kärger, D.M. Ruthven, J. Phys. Chem. C 122 (2018) 7217.
[108] P. Cnudde, E.A. Redekop, W. Dai, N.G. Porcaro, M. Waroquier, S. Bordiga, M. Hunger, L. Li, U. Olsbye, V. Van Speybroeck, Angew Chem. Int. Ed. Engl. 60 (2021) 10016–10022.
[109] A.O. Koriabkina, A.M. de Jong, D. Schuring, J. van Grondelle, R.A. van Santen, J. Phys. Chem. B 106 (2002) 9559.
[110] C.T. Campbell, J.R.V. Sellers, J. Am. Chem. Soc. 134 (2012) 18109.
[111] L.H. Sprowl, C.T. Campbell, L. Árnadóttir, J. Phys. Chem. C 120 (2016) 9719.
[112] H. Li, C. Paolucci, W.F. Schneider, J. Chem. Theor. Comput. 14 (2018) 929.
[113] T. Bucko, J. Hafner, J. Phys. Condens. Matter 22 (2010) 384201.
[114] B.A. De Moor, A. Ghysels, M.-F. Reyniers, V. Van Speybroeck, M. Waroquier, G. B. Marin, J. Chem. Theor. Comput. 7 (2011) 1090.
[115] C.G. Pope, J. Phys. Chem. 88 (1984) 6312.
[116] C.G. Pope, J. Phys. Chem. 90 (1986) 835.
[117] P.J. Dauenhauer, O.A. Abdelrahman, ACS Cent. Sci. 4 (2018) 1235.
[118] V. Van Speybroeck, J. Van der Mynsbrugge, M. Vandichel, K. Hemelsoet, D. Lesthaeghe, A. Ghysels, G.B. Marin, M. Waroquier, J. Am. Chem. Soc. 133 (2011) 888.
[119] C.-M. Wang, Y.-D. Wang, Z.-K. Xie, Chin. J. Catal. 39 (2018) 1272.
[120] C.-M. Wang, Y.-D. Wang, H.-X. Liu, G. Yang, Y.-J. Du, Z.-K. Xie, Chin. J. Catal. 36 (2015) 1573.